공학석사 학위논문

Double-Side Passivation of Perovskite Solar Cells for High Performance and Stability

양 계면 결함제어 공정을 통한 고성능 및 고안정성 페로브스카이트 광전소자 구현

2023년 8월

서울대학교 공과대학원
재료공학부
김 범 수

Double-Side Passivation of Perovskite Solar Cells for High Performance and Stability

양 계면 결함제어 공정을 통한 고성능 및

고안정성 페로브스카이트 광전소자 구현

지도 교수 박 병 우

이 논문을 공학석사 학위논문으로 제출함

2023년 8월

서울대학교 공과대학원

재료공학부

김 범 수

김범수의 공학석사 학위논문을 인준함

2023년 8월

위 원 장	장 호 원	(인)
부위원장	박 병 우	(인)
위 원	이 명 재	(인)
위 원	김 진 현	(인)

Abstract

Organic-inorganic hybrid Perovskite solar cells (PSCs) are in the spotlight as promising renewable energy devices due to their desirable properties. However, they face challenges concerning both power conversion efficiency (PCE) and long-term stability. The presence of surface defects in PSCs poses a major hurdle to achieving high efficiency and stability, as these defects cause nonradiative recombination and degradation.

Thus, suppressing electronic defects in both interfaces between the charge carrier transport layers and the perovskite layer is essential to improve photovoltaic performance and the long-term stability of PSCs. Herein, a novel double-side surface passivation method using phenyltrimethylammonium iodide (PTMAI) salt is applied to remove electronic defects effectively. PTMA cation is a quaternary ammonium salt known for its resistance to water and thermal stress as an effective defect passivator. Moreover, the bulky nature of this cation helps to suppress ion migration through the perovskite layer toward interfaces between the perovskite and charge transport layer.

As a result, double-side passivation with PTMAI contributes to the enhancement of the perovskite crystallinity with the relaxed nonuniform distribution of the local strain of the perovskite layer. Furthermore, this passivation method also achieves remarkable suppression of trap density, promoting the growth of larger grains and a smoother surface in the perovskite layer. Consequently, the efficiency of formamidinium lead iodide ($FAPbI_3$) PSC is significantly improved by double-side passivation with PTMAI, achieving a PCE of 21.87%. Moreover, the passivated cell exhibited enhanced long-term stability, maintaining over 80% of its initial PCE after 1860 h and 1030 h under 60 ℃ and continuous 1 sun illumination, respectively.

Keywords: perovskite solar cells, defect passivation, double-side passivation, phenyltrimethylammonium iodide, long-term stability

Student Number: 2021-29138

Table of Contents

List of Figures

Chapter 1.

Chapter 2.

Chapter 1.

Introduction to Overview of Perovskite Photovoltaics

1.1. Introduction to Solar Cells

Solar cells harness the photovoltaic effect of materials to convert solar energy into electrical power. This process begins with the absorption of photons in the material, which generates electron-hole pairs in Figure 1-1 [1]. The charge transport layer material facilitates the separation of these electron-hole pairs and collects the charges produced by the light-absorbing material. The potential difference between the anode and cathode creates an electric field that drives the flow of current, thus generating electrical power [1-2].

To characterize the photovoltaic performance of solar cells, three key parameters are typically considered: short-circuit current (J_{SC}), open-circuit voltage (V_{OC}), and fill factor (FF) depicted in Figure 1-2. The power conversion efficiency (PCE) of a solar cell is defined as the ratio between the maximum power output ($V_{MPP} \times J_{MPP}$) of a solar cell and the input power of incident light. Maximum power output is calculated by the product of J_{SC}, V_{OC}, and FF. The fill factor is the ratio between PCE (η) and the product of J_{SC} and V_{OC}, which is the area ratio between A and B in Figure 1-2. In general, semiconductors with lower bandgaps tend to have higher J_{SC}, as they absorb a larger portion of the incident light. On the other hand, semiconductors with higher bandgaps exhibit higher V_{OC}, as they create a larger potential difference. The tradeoff between J_{SC} and V_{OC} sets the theoretical limit of solar cells, known as the Shockley-Queisser limit, as shown in Figure 1-3 [3]. Therefore, optimizing the bandgap of the light-harvesting material is crucial, and a bandgap ranging from 1.2 to 1.5 eV is considered favorable for achieving high PCE.

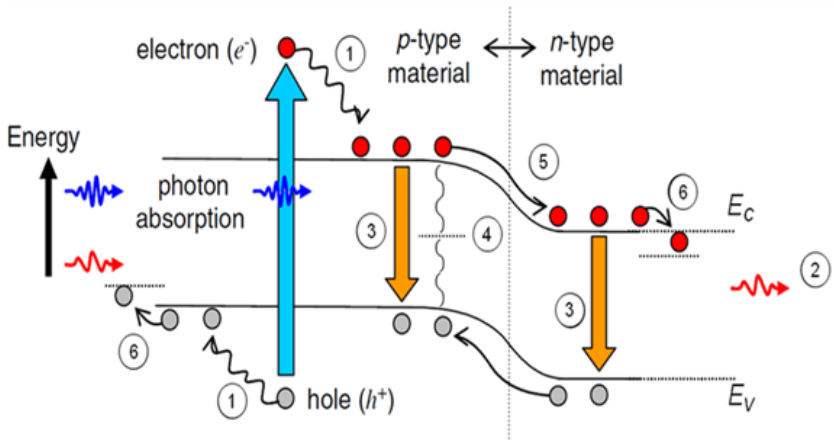

Figure 1-1. Operation process of *p-n* junction solar cells. From Ref. [1].

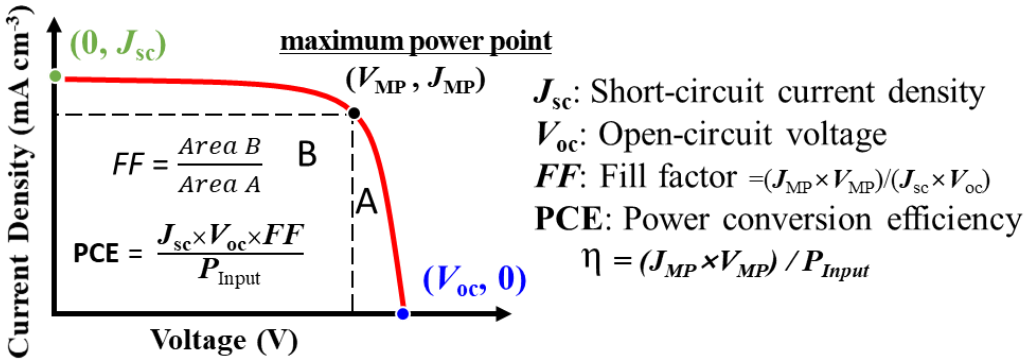

Figure 1-2. Schematic of *J*-*V* curve and definition of photovoltaic parameters to evaluate the photovoltaic performance of solar cells.

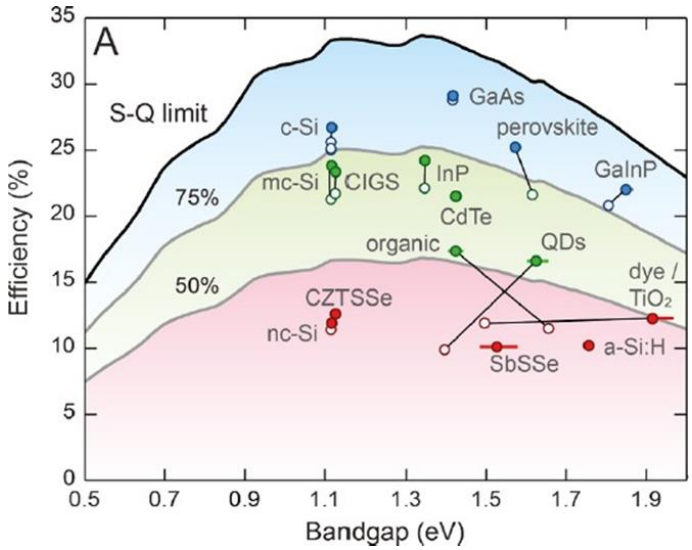

Figure 1-3. Limitation for real-world photovoltaic devices. Shockley-Queisser efficiency limits and record efficiencies of various solar cells against their bandgap. From Ref. [3].

1.2. Basic Structure of Perovskite Solar Cells

Perovskite Solar Cells (PSCs) are typically composed of an ABX_3 structure, where A represents an organic cation such as formamidinium ($(NH_2)_2CH^+$ (FA^+)) or methylammonium ($CH_3NH_3^+$ (MA^+)), B represents a metal cation such as Pb, Sn, and X represents a halide anion in Figure 1-4 [4]. The composition of PSCs can be engineered by incorporating various cations and anions at each A, B, and X site. To predict the preferred structure, a parameter known as the Goldschmidt tolerance factor (t) is commonly used [5-7].

the Goldschmidt tolerance factor is a dimensionless parameter value that quantifies the distortion of strain in the crystal structure of perovskite materials. It is calculated from the ionic radius of the atoms involved, specifically the radius of the A cation (r_A), the radius of the B cation (r_B), and the radius of the X anion (r_X) in Figure 1-5. In the inorganic-organic hybrid perovskite materials, the orthorhombic structure is typically observed with a tolerance factor lower than 0.8, a cubic structure ranging from 0.8 to 1.0, and a hexagonal structure with a tolerance factor higher than 1.0 [5]. Researchers often manipulate the composition of the perovskite precursor within the appropriate range of tolerance factors to achieve optimized photovoltaic devices with high power conversion efficiency (PCE) and long-term stability.

Perovskite solar cells are fabricated using low-temperature solution methods, which allows for the fabrication of perovskite solar cells with diverse structures, including *n-i-p* mesoscopic, *n-i-p* planar, *p-i-n* mesoscopic, or *p-i-n* planar configurations as shown in Figure 1-6 [8]. This characteristic opens up possibilities for various applications of PSCs.

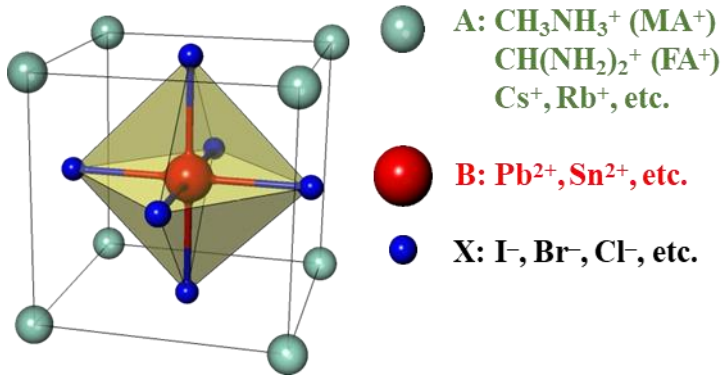

Figure 1-4. Schematic of ABX_3 perovskite crystal structure.

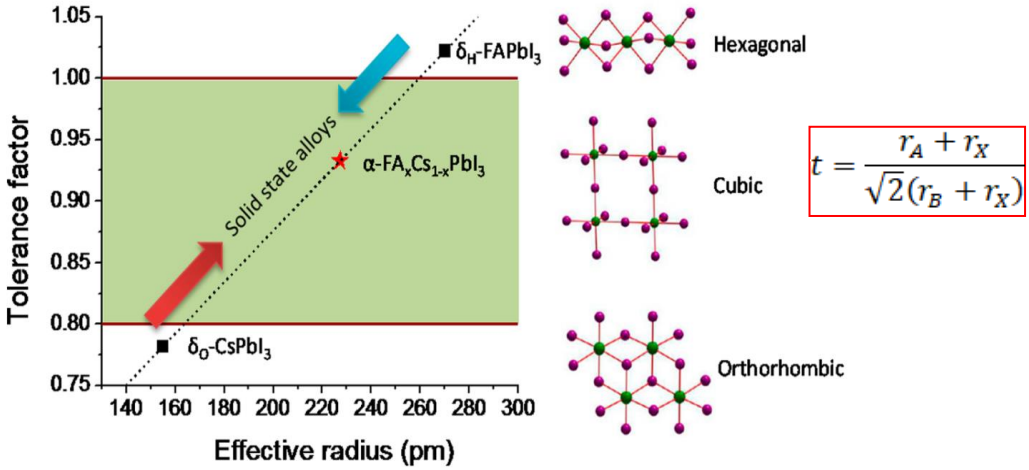

Figure 1-5. Structure stability according to correlations between tolerance factor and crystal structure of perovskite materials. From Ref. [5].

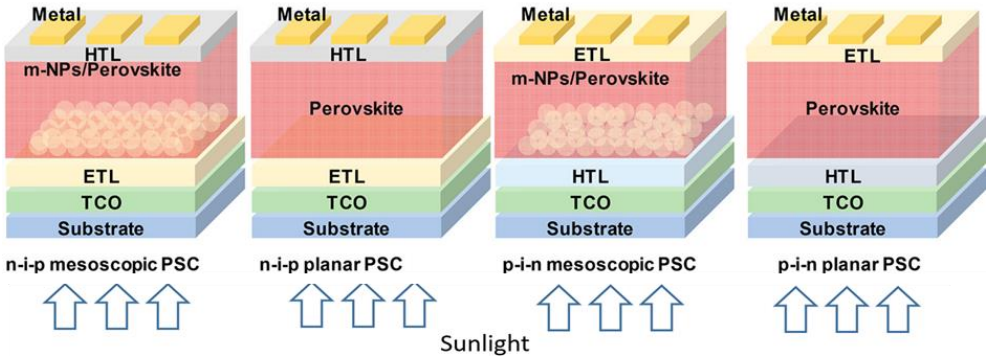

Figure 1-6. Various device architectures of perovskite solar cells. From Ref. [8].

1.3. Advantages and Disadvantages of Perovskite Solar Cells

PSCs have gained attention as a potential option for sustainable energy devices with various advantages for suitable solar cells. First of all, a simple solution process with an antisolvent method is used for the fabrication of PSCs without a vacuum process in Figure 1-7 [9]. It has a lower temperature process with uniform crystallization of perovskite film, which leads to high price competition for commercialization in the solar cell market.

Moreover, the bandgap of PSCs can be tunable with the composition engineering of perovskite precursor. according to the need for proper bandgap design in Figure 1-8 [10-11]. This advantage allows the possibilities of efficiency and performance in multi-junction solar cells by combining designed proper bandgap perovskite cells with other photovoltaic devices. Additionally, perovskite materials have superior light absorption coefficient ($>10^4$ cm^{-1}) [12] and long charge carrier diffusion length (~175 μm for a single crystal $MAPbI_3$) in Figure 1-9 [13-14].

Despite the advantages of desirable properties of perovskite solar cells, the fragility of weak hydrogen interactions between the organic sites and halide sites make perovskite optoelectronics susceptible to degradation caused by external factors such as light, water, and heat in Figure 1-10 [15-17]. Furthermore, the volatility of the organic A cation and halide X anion in perovskite makes it susceptible to defect formation during the solution process and annealing steps. These defects, such as ionic substitutions, interstitials, and vacancies, can lead to non-radiative recombination, trap state formation, and reduced carrier mobility, which can lower not only the photovoltaic performance but also the long-term stability of PSCs [18-20].

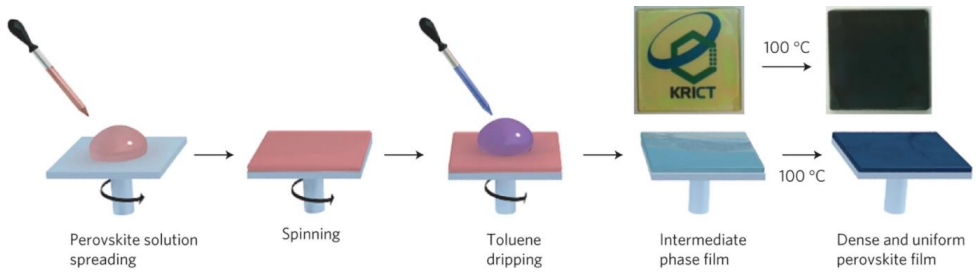

Figure 1-7. Simple solution process with the antisolvent method for fabrication of perovskite solar cells. From Ref. [9].

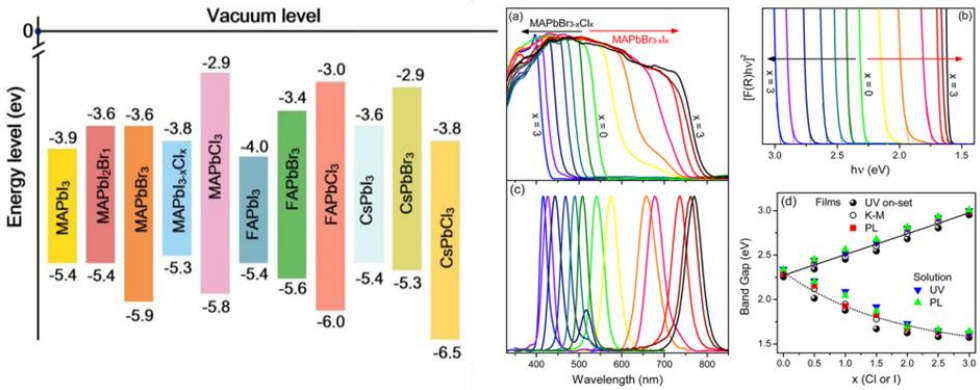

Figure 1-8. Bandgap tunability of PSCs (ABX_3). From Ref. [10-11].

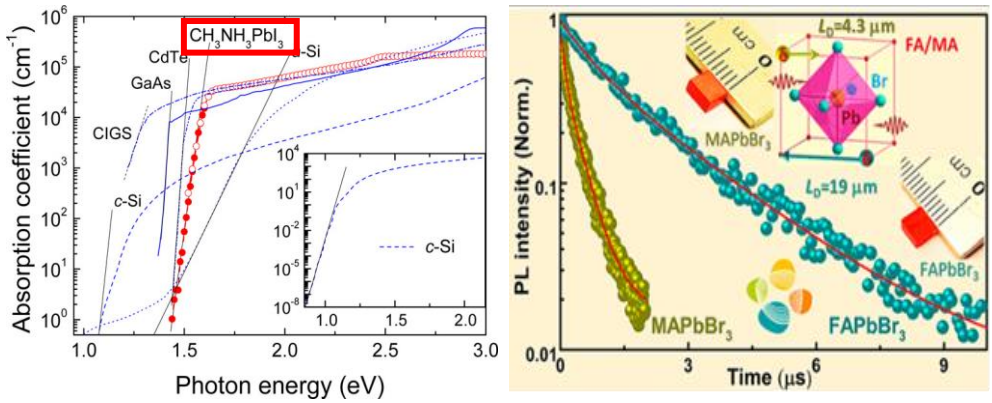

Figure 1-9. High absorption coefficients and long charge carrier diffusion length of PSCs. From Ref. [12-13].

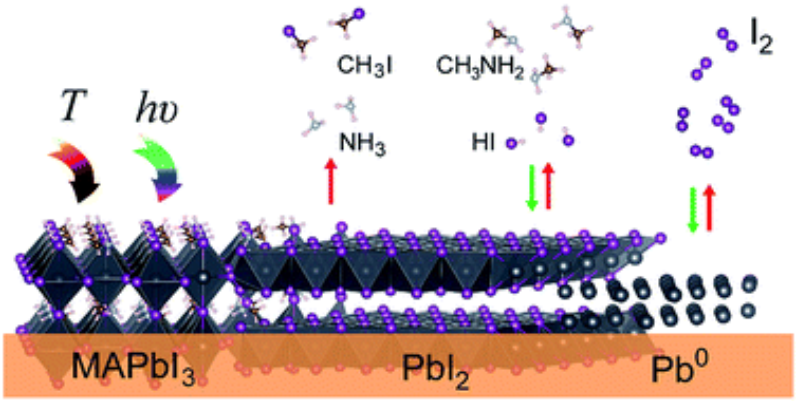

Figure 1-10. Degradation process in $MAPbI_3$ solar cell. From Ref. [15].

1.4. References

[1] G. E. Arnaoutakis, *Degree Thesis*, Heriot-Watt University, Edinburgh, Scotland, June, **2015**.

[2] M. Shanawani, D. Masotti, A. Costanzo, *Electronics* **2017**, *6*, 99.

[3] E. Bruno, A.-L. Esther, W. T. Stefan, V. Tom, C. G. Erick, P. Albert, *ACS Energy Lett.* **2020**, *5*, 3029.

[4] A. Kojima, K. Teshima, Y. Shirai, T. Miyasaka, *J. Am. Chem. Soc*. **2009**, *131*, 6050.

[5] Z. Li, M. Yang, J.-S. Park, S.-H. Wei, J. J. Berry, K. Zhu, *Chem. Mater.* **2016**, *28*, 284.

[6] G. Kieslich, S. Sun, A. K. Cheetham, *Chem. Sci*. **2015**, *6*, 3430.

[7] V. M. Goldschemidt, *Naturwissenschaften* **1926**, *14*, 477.

[8] H. Li, W. Zhang, *Chem. Rev*. **2020**, *120*, 9835.

[9] N. J. Jeon, J. H. Noh, Y. C. Kim, W. S. Yang, S. Ryu, S. I. Seok, *Nat. Mater.* **2014**, *13*, 897.

[10] Y. Wu, W. Chen, G. Chen. L. Liu, Z. He, R. Liu, *Nanomaterials* **2018**, *8*, 356.

[11] H. Li, W. Zhang, *Chem. Rev*. **2020**, *120*, 9835.

[12] S. D. Wolf, J. Holovsky, S.-J. Moon, P. Löper, B. Niesen, M. Ledinsky, F.-J. Haug, J.-H. Yum, C. Ballif, *J. Phys. Chem. Lett.* **2014**, *5*, 1035.

[13] A. A. Zhumekenov, M. I. Saidaminov, M. A. Haque, E. Alarousu, S. P. Sarmah, B. Murali, L. Dursun, X.-H. Miao, A. L. Abdelhady, T. Wu, O. F. Mohammed, O. M. Bakr, *ACS Energy Lett.* **2016**, *1*, 32.

[14] Q. Dong, Y. Fang, Y. Shao, P. Mulligan, J. Qiu, L. Cao, J. Huang, *Science* **2015**, *347*, 6225.

[15] E. J. Juarez-Perez, L. K. Ono, M. Maeda, Y. Jiang, Z. Hawash, Y. Qi, *J. Mater. Chem. A* **2018**, *6*, 9604.

[16] G. Divitini, S. Cacovich, F. Matteocci, L. Cinà, A. D. Carlo, C. Ducati, *Nat. Energy* **2016**, *1*, 15012.

[17] J. M. Frost, K. T. Butler, F. Brivio, C. H. Hendon, M. V. Schilfgaarde, A.

Walsh, *Nano Lett*. **2014**, *14*, 2584.

[18] C. S. Ponseca, Jr, T. J. Savenije, M. Abdellah, K. Zheng, A. Yartsev, T. Pascher, T. Harlang, P. Chabera, T. Pullerits, A. Stepanov, J.-P. Wolf, V. Sundström, *J. Am. Chem. Soc.* **2014**, *136*, 5189.

[19] B. Chen, P. N. Rudd, S. Yang, Y. Yuan, J. Huang, *Chem. Soc. Rev.* **2019**, *48*, 3842.

[20] Y. Yuan, J. Huang, *Acc. Chem. Res.* **2016**, *49*, 286.

Chapter 2.

Double-Side Passivation of Perovskite Solar Cells for High Performance and Stability

2.1. Introduction

Despite the promising optical and electrical properties of perovskite for next-generation photovoltaics, there remain significant challenges and unresolved issues hinder their widespread adoption in next-generation photovoltaics. These challenges include the need to suppress the interfacial and bulk defects in perovskite, enhance the charge-exchanging ability of the electron transport layer (ETL) and hole transport layer (HTL), and achieve long-term reliability [1-5].

Surface passivation is a potential approach to improve both the photovoltaic performance and stability of PSCs by suppressing defects in the light absorption layer [6-8]. Among the surface treatment materials, organic halide salt is mainly used for the posttreatment of PSCs due to its similarity with the organic cation of perovskite constituent. Phenyltrimethylammonium (PTMA) halide material is one of the organic halide passivators with high hydrophobicity, thermal stability, and strong interaction with the perovskite layer according to its structure of quaternary ammonium salt [9-10]. Despite the positive effects of PTMA passivation on stability and performance, the long-term stability data are still scarce under continuous light and thermal stress conditions.

Herein, we develop sequential double-side passivation with phenyltrimethylammonium iodide (PTMAI) between both the carrier transport layers and the perovskite layer, which are ETL/perovskite and perovskite/HTL interfaces, respectively [11-13]. In this method, PTMAI can passivate the bottom- and top- side surface defects of the perovskite layer. With the bottom-side passivation, it has a smoother surface and larger grain size compared with the nonpassivated perovskite film. Furthermore, double-side passivation with PTMAI has a synergetic impact on both the morphological and electrical properties of the

perovskite layer. As a result, formamidinium lead iodide ($FAPbI_3$) PSC with double-side passivation achieved an efficiency of 21.87%, along with retention of 86.4% compared to initial efficiency after 1860 h of 60 ℃ thermal stress and retention of 80.2% compared to initial efficiency after 1030 h at continuous 1 sun illumination (AM 1.5G).

2.2. Experimental Section/Methods

***Perovskite Solution Preparation*:** To prepare the $FAPbI_3$ perovskite precursor solution, formamidinium iodide (223.56 mg, FAI, GreatCell Solar), lead iodide (599.31 mg, PbI_2, TCI Chemicals), and methylammonium chloride (36.11 mg, MACl, Sigma-Aldrich) were dissolved into a mixture of *N*,*N*-dimethylformamide (857.14 µL, DMF, Sigma-Aldrich) and dimethyl sulfoxide (142.86 µL, DMSO, Sigma-Aldrich) at a 6:1 volume ratio.

***Solar Cell Fabrication*:** For cleaning the ITO/glass substrates (AMG), the sonication step was conducted by sequential 30 min socking in acetone, isopropyl alcohol, and deionized water. Then, the sonicated substrates underwent a UV-ozone treatment for 15 min. To prepare the Tin(II) oxide (SnO_2) nanoparticle solution, a SnO_2 colloidal dispersion (Alfa-Aesar) was diluted with deionized water at a 1:4 volume ratio. Subsequently, the diluted SnO_2 solution was spin-coated onto the UV-ozone-treated substrates at 3000 rpm for 30 s. The coated substrates were then annealed at 120 ℃ for 30 min. Once the substrates had cooled down, the SnO_2-coated substrates underwent additional UV-ozone treatment for 15 min. For the *Bottom* and *Double* devices, phenyltrimethylammonium iodide (0.05 mg mL^{-1}, PTMAI, TCI Chemicals) precursor in 2-propanol (IPA, Dae-Jung) was spin-coated onto the SnO_2-coated substrates at 4500 rpm for 30 s, followed by annealing at 100 ℃ for 5 min. Next, the perovskite precursor solution was deposited in the ambient air, following 2 steps of spin-coating: The first step involved spinning the solution at 1000 rpm for 30 s, followed by a second step at 5000 rpm for 10 s. As an antisolvent, ethyl ether (1.0 mL, Dae-Jung) was carefully dropped onto the spinning substrates at 1 s after the beginning of the second step. Subsequently, perovskite-coated substrates were annealed at 150 ℃ for 10 min. For the *Top* and *Double* devices, a PTMAI solution (0.5 mg mL^{-1} in IPA) was spin-coated onto the perovskite films at 4500 rpm for 30 s. The coated substrates were annealed at 100 ℃ for 5 min. To prepare spiro-OMeTAD solution as an HTL, spiro-OMeTAD (72.3 mg mL^{-1}, Lumetec) was dissolved into chlorobenzene (1 mL, CB, Sigma-Aldrich) by incorporating 4-*tert*-butyl pyridine (28.8 µL, *t*BP, Sigma-Aldrich), lithium bis(trifluoromethanesulfonyl)imide (17.5 µL, Li-TFSI, Sigma-Aldrich)

solution (520 mg mL^{-1} in acetonitrile), and Co (II)-TFSI (21.9 μL, FK209, Sigma-Aldrich) solution (384 mg mL^{-1} in acetonitrile) as additives. The spiro-OMeTAD solution was spin-coated onto the substrates at 3000 rpm for 30 s. For the device of long-term stability test, poly[bis(4-phenyl)(2,4,6-trimethylphenyl)amine] (17.5 mg mL^{-1}, PTAA, 117 kDa, MS Solution) was dissolved in CB (1 mL) with *t*BP (6 μL) and Li-TFSI solution (4 μL) to prepare PTAA solution. PTAA solution was spin-coated onto perovskite films at 3000 rpm for 30 s. Lastly, the Au electrode was thermally evaporated to complete the PSC devices. For long-term stability tests, PSCs were encapsulated by capping glass the glass substrates using a UV-light-curing epoxy resin (XNR-580, Nagase).

***Characterization*:** Current-Voltage (*J*-*V*) characteristic measurement was conducted with the solar simulator (K3000, McScience) under 1 sun illumination (100 mW cm^{-2}) as a standard of AM 1.5G. X-ray diffractometer (New D8 Advance, Bruker) was conducted to perform phase analysis on the perovskite film. X-ray photoelectron spectroscopy (K-Alpha plus, Thermo Fisher Scientific) was used to perform chemical analysis on the perovskite film, and grazing-incidence x-ray diffraction (GIXRD, XEUSS2.0, Xenocs) was conducted with Cu Kα x-ray radiation. To account for instrumental broadening, the obtained Δk_z vs. k_z plot was calibrated using a resolution function derived from a standard silicon powder, which was determined as $2.4752 \times 10^{-4}\ k_z + 0.02712\ nm^{-1}$. Atomic force microscopy (AFM, NX-10, Park Systems) was employed for surface roughness analysis. To analyze the cross-sectional and surficial morphology of the full devices and perovskite film, a scanning electron microscope (Merlin Compact (FE-SEM), ZEISS) was utilized. UV-vis spectrophotometer (V-770, Jasco) was conducted to analyze absorption spectra and optical bandgap of perovskite. Steady-state and time-resolved photoluminescence (PL) measurements were performed with a fluorescence spectrometer (FlouTime 300, PicoQuant) to analyze the optoelectronic properties of perovskite films. Potentiostat (Zive SP-1, WonATech) was performed for obtaining the impedance of PSCs through 10 mV AC voltage with verifying frequency in the dark state, which led to capacitance data for trap analysis. For a long-term stability test, both temperature-controlled and continuous light-emitting environments were required. The thermal stability test was conducted in a temperature-controlled chamber (TH-PE-025, JeioTech) at

60 °C. Maximum power point tracking (MPPT) was conducted with a solar cell reliability test system (K3600, McScience) under 1 sun illumination (AM 1.5 G) during an applied constant maximum-power bias.

2.3. Results and Discussion

Four types of devices were prepared with different passivation methods to investigate the effects of PTMAI passivation on interfaces of perovskite layer. These devices are denoted as "*Control*" ($FAPbI_3$), "*Bottom*" (PTMAI/$FAPbI_3$), "*Top*" ($FAPbI_3$/PTMAI), and "*Double*" (PTMAI/$FAPbI_3$/PTMAI). The schematic diagram in Figure 2-1(a) depicts the fabrication process of the double-side passivated device with PTMAI. To minimize possible perovskite damage, different annealing conditions were employed for PTMAI passivation with 100 ℃, which is adapted for evaporating solvent while preventing the degradation of organic halide, and the perovskite synthesis at 150 ℃ due to the temperature requirements for the high-quality cubic-phase $FAPbI_3$ [14-17]. Figure 2-1(b) shows that the introduction of the PTMAI salt into the interfaces contributes to the enhancement of the photovoltaic performance. While the change of the J_{SC} is not significant, remarkable enhancements in V_{OC} and *FF* are observed, which leads to an overall increase in PCE. To understand the improvement of V_{OC}, *FF*, and PCE, in-depth studies of phase and nonuniform distribution of local strains are conducted.

Since the PTMAI is located on the both bottom and top sides of the perovskite layer, phase and bulk properties of perovskite may change. X-ray diffraction (XRD) was conducted for the perovskite crystalline structure in Figure 2-2. It shows that the characteristic peak of the perovskite exhibits a negligible difference between the *Control* and passivated perovskite films. However, there is a noticeable enhancement in the peak intensity of the (001) plane, which increases in the order of *Control*, *Bottom*, *Top*, and *Double* films. This observation suggests that the passivation with PTMAI can improve the crystallinity of the perovskite film. This enhanced crystallinity might be attributed to the decreased defects at the bottom-side interface of the perovskite layer, which leads to the improved arrangement and alignment of perovskite-phase crystallizations.

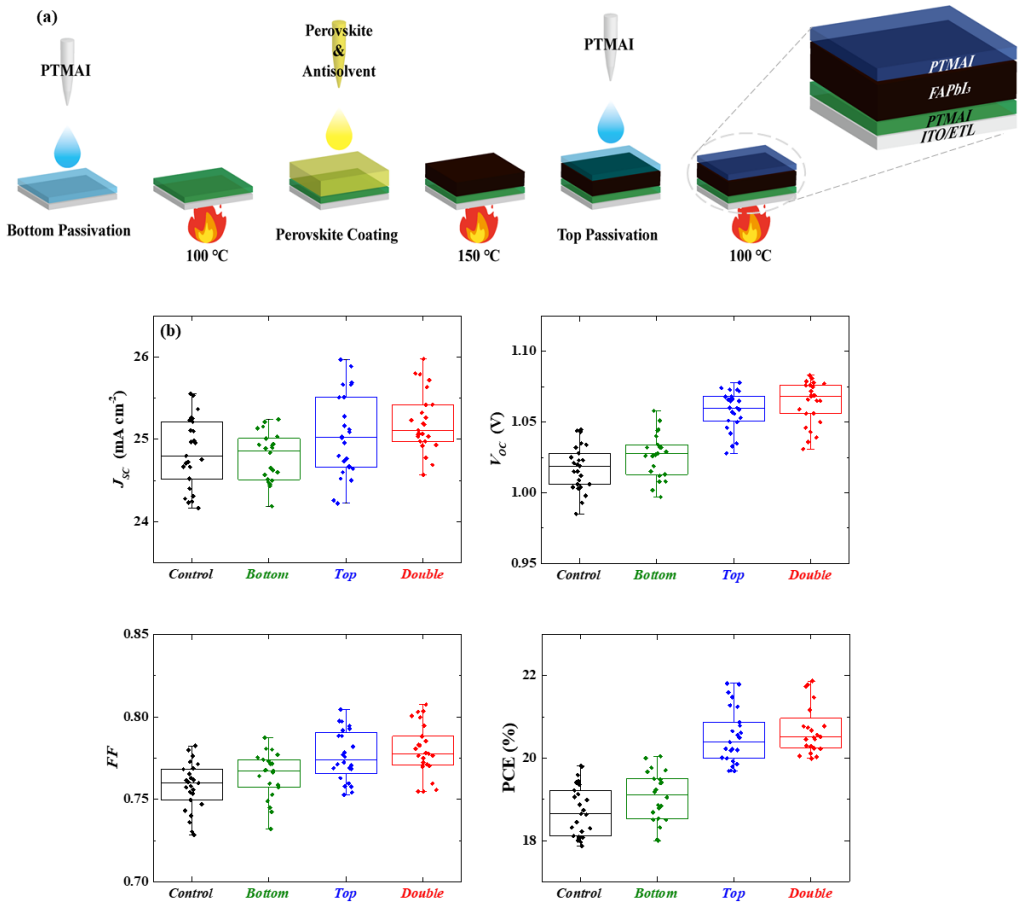

Figure 2-1. Fabrication procedure and statistical distribution of the photovoltaic performances of PSCs. (a) Schematics for the double-side passivated PSCs. (b) Performances of J_{SC}, V_{OC}, FF, and PCE for the $FAPbI_3$-based solar cells without/with the passivation of PTMAI.

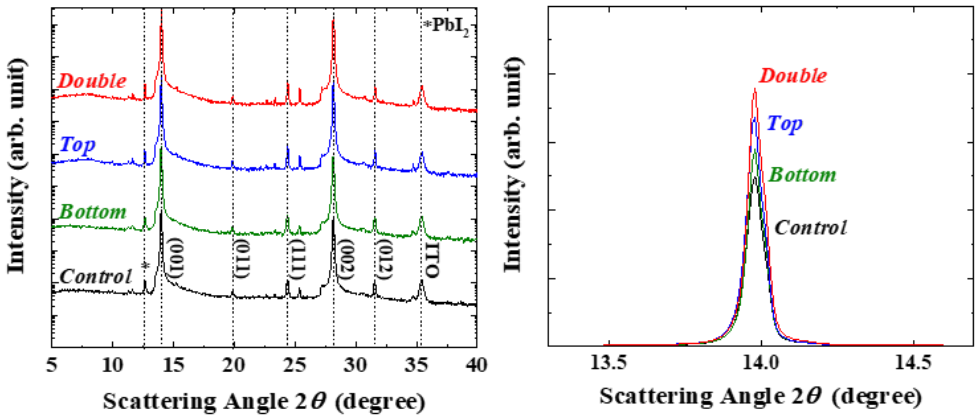

Figure 2-2. X-ray diffraction of the perovskite films. XRD patterns and peak intensity of the (001) plane of *Control*, *Bottom*, *Top*, and *Double* films.

To further study the reason for the improved crystallinity of perovskite films by PTMAI passivation, x-ray photoelectron spectroscopy (XPS) was conducted. Figure 2-3 illustrates the XPS spectra of Pb 4*f* peaks and I 3*d* peaks indicating that PTMAI causes discernible changes in binding energies of Pb 4*f* and I 3*d*. Specifically, XPS peaks shift slightly towards lower binding energy with the presence of PTMAI passivation layers. The results indicate that the addition of PTMAI brings modification of the bonding state within the perovskite film. PTMAI acts as a bulky passivator, effectively passivating I vacancies [18-20]. Despite its bulky nature, this suggests that the bonding length of Pb-I has increased without creating any additional metallic Pb [20-23].

For a deeper understanding as to how PTMAI influences the perovskite layer, grazing-incidence x-ray diffraction (GIXRD) was utilized. It can be inferred that the surface passivation with PTMAI contributes to the formation of 2D perovskite in a direction perpendicular to the plane, which was confirmed by the GIXRD data of the *Top* and *Double* films in Figure 2-4. The relaxed layered crystal structure of 2D hybrid perovskite, caused by axial halides, makes it distinct from 3D perovskite [24-25]. Consequently, the Pb-I bond in 2D perovskite becomes longer than that in 3D perovskite. This observation is also supported by the downward shift of Pb 4*f* towards low binding energy.

The nonuniform distribution of local strains of the perovskite film is extracted from the Δk_z vs. k_z plot (with the scattering vector $k_z = (4\pi/\lambda) \sin \theta$, by converting the θ–2θ diffraction data into in Figure 2-5 [26-32]. The nonuniform distribution of local strains in the perovskite films follows a decreasing trend in the order of the *Control*, *Bottom*, *Top*, and *Double* films. Notably, the *Top* perovskite film demonstrates a significant reduction in the local strains compared to the *Control* film, indicating that the incorporation of the 2D perovskite effectively mitigated defective local strains within the perovskite lattice. These observations suggest that the treatment of PTMAI can facilitate a formation of tightly-packed and aligned perovskite lattice, resulting in the reduced local strains. To gain a more comprehensive understanding of the decrease in the defects within the perovskite film, it is crucial to conduct thorough morphological analyses.

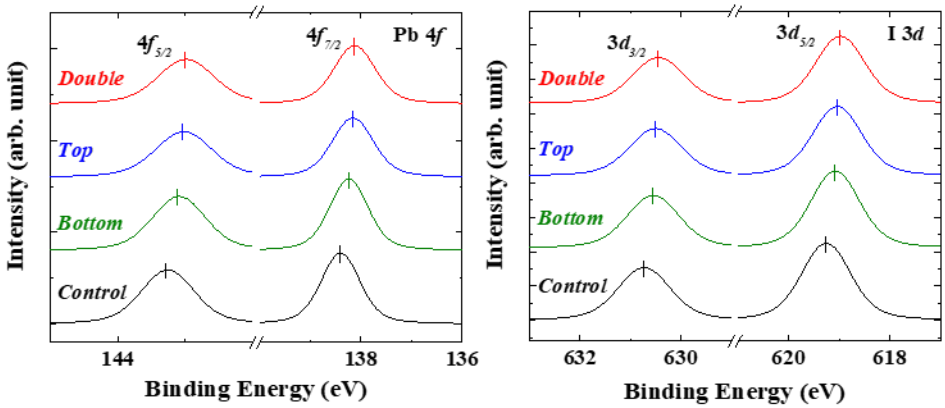

Figure 2-3. X-ray photoelectron spectroscopy (XPS) of the perovskite films. XPS spectra of Pb 4*f* and I 3*d* confirming the binding energy shift.

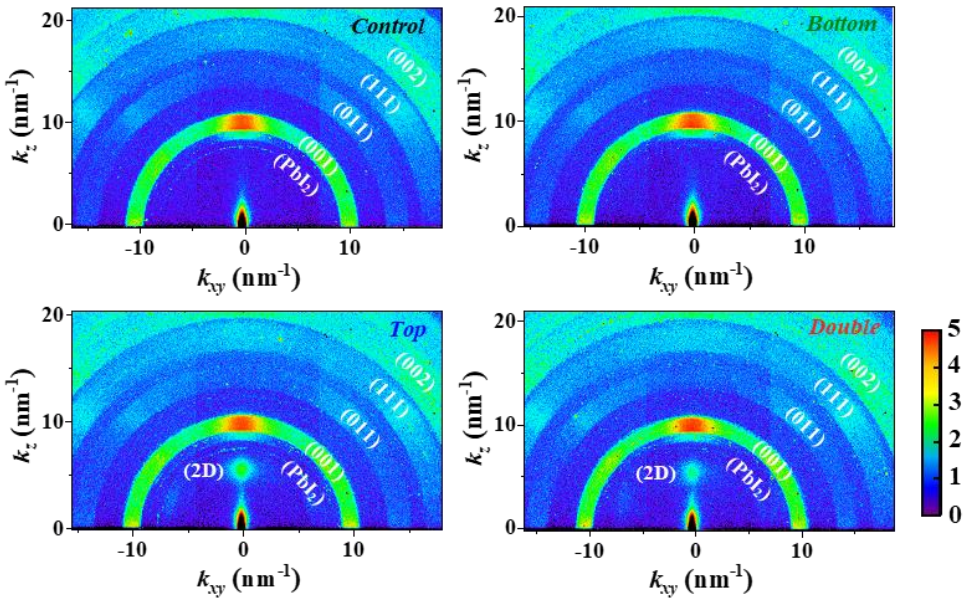

Figure 2-4. Grazing-incidence x-ray diffraction (GIXRD) in the perovskite film. GIXRD with Cu Kα x-ray radiation in the perovskite film with various conditions of PTMAI passivation.

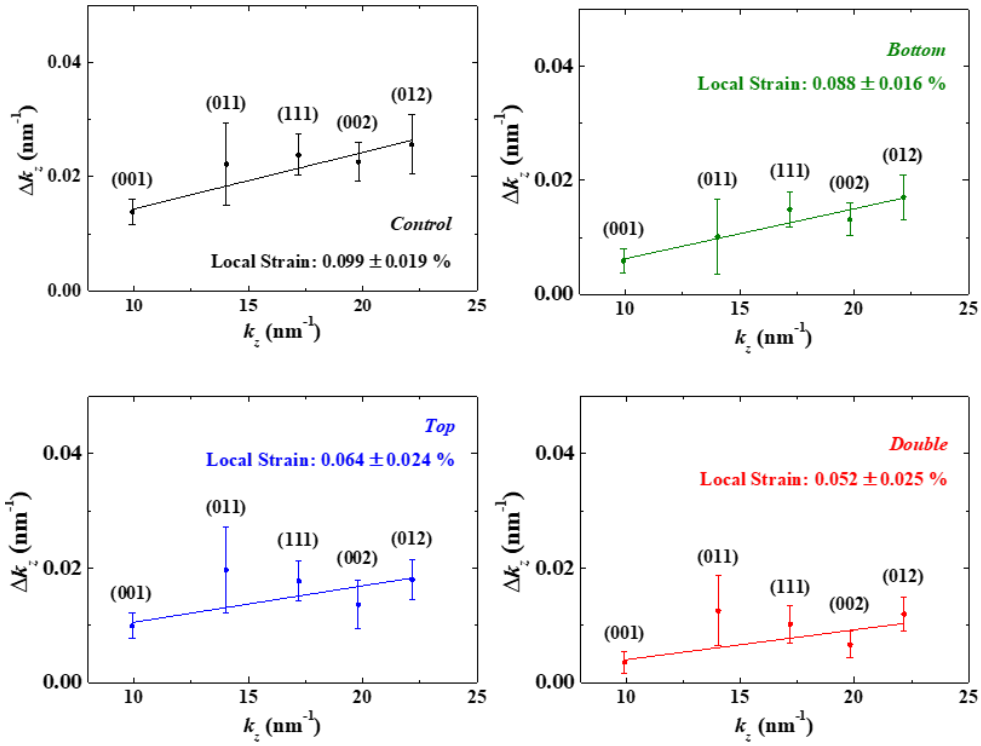

Figure 2-5. Nonuniform distribution of local strains in the perovskite films. Δk_z vs. k_z plot obtained from the θ–2θ x-ray diffraction for the nonuniform distribution of local strains in the perovskite films.

Atomic force microscopy (AFM) was employed for surface roughness analysis. Figure 2-6(a) demonstrates that the surface roughness exhibits decreasing trend in the order of *Control*, *Bottom*, *Top*, and *Double* films, implying that the introduction of PTMAI results in a reduction in the surface roughness of the perovskite layer. These findings indicate that incorporating PTMAI leads to a smoother surface of the perovskite layer, facilitating improved contact with HTL. This improved surface contact between the perovskite layer and HTL is beneficial for enhancing the photovoltaic performance of the PSCs.

Scanning electron microscopy (SEM) was utilized for the cross-sectional and plan-view analyses of perovskite films to analyze the surface morphology according to the effect of double-side passivation with PTMAI. In Figure 2-6(b) the cross-sectional view reveals that the *Double* cell exhibits a better pinhole-free image, smoother interface, and larger grain size than the other devices. In Figure 2-6(c), plan-view SEM images show a noticeable increase in the lateral grain size of perovskite with PTMAI, which is also shown in Figure 2-6(d). Notably, the grain size of the perovskite exhibits a progressive increase in the order of the *Control*, *Bottom*, *Top*, and *Double* films. The *Double* film features the largest grains, resulting in an average size of ~1150 nm. The observed grain-size increase aligns with the enhanced crystallinity, evident in the x-ray analyses in Figures 2-2.

To analyze the optoelectronic properties of the perovskite film, absorption and photoluminescence (PL) measurements were conducted. Figure 2-6(e) shows that the *Control* and PTMAI-passivated films have almost the same optical bandgap of ~1.54 eV, which is similar to the state-of-the-art $FAPbI_3$-based perovskite film [33]. However, PL spectra in Figure 2-6(f) suggest that PTMAI effectively passivates electronic defects, leading to enhanced photoexcitation. Moreover, the time-resolved PL in Figure 2-6(g) confirms that the double passivation of PTMAI induces a longer carrier lifetime, which is highly favorable for solar cell performance.

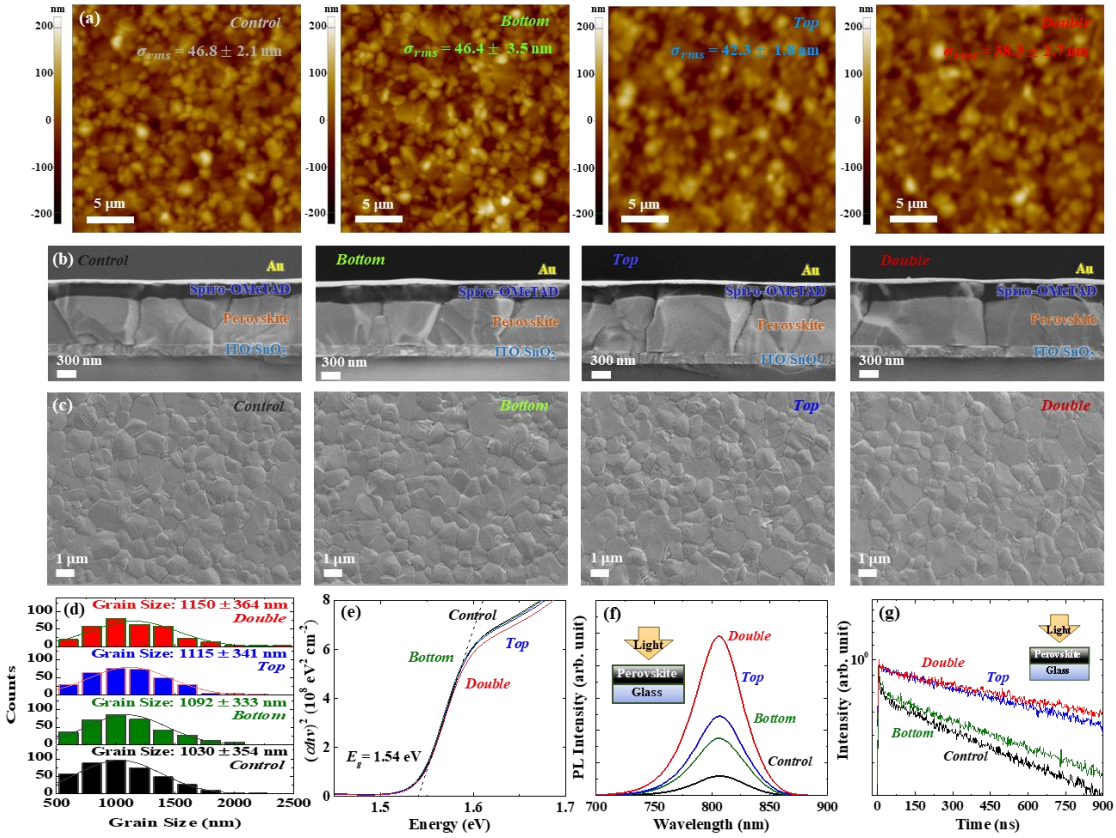

Figure 2-6. Surface morphology and optoelectronic properties of perovskite films. (a) AFM images, (b) cross-sectional SEM images, (c) plan-view SEM images, and (d) lateral grain size distributions of the *Control*, *Bottom*, *Top*, and *Double* films. (e) UV-vis absorption, (f) steady-state PL, and (g) time-resolved PL spectra of the perovskite films.

Previous studies have shown that the top PTMA layer can effectively suppress surface defects of the perovskite layer, leading to enhanced efficiencies compared to controls [9,10,34-35]. However, this approach has limitations in that it can only address defects present at the perovskite/HTL interface. To overcome this limitation, we have introduced a double-side passivation to control the defects present at both interfaces in contact with the perovskite layer. The effectiveness of this approach is confirmed by decreased electronic trap density extracted from the electrochemical impedance spectroscopy (EIS) depicted in Figure 2-7(a).

This facile and effective approach by implementing double-side passivation using PTMAI results in the improved efficiency and stability of PSCs. Figure 2-7(b) shows that the photovoltaic performance is the best with the PCE of 21.87% for the *Double* device, which is compared to the 19.81%, 20.05%, 21.81%, respectively, for the *Control*, *Bottom*, *Top* devices. As previously mentioned, the incorporated PTMAI in the perovskite layer serves as a defect passivator, reducing defects, trap densities, and non-recombination sites, which leads to optimized optoelectronic performance as well as high photovoltaic performance.

The lack of long-term stability under light and heat has impeded the commercialization of PSCs. there is an increasing requirement for achieving reliable stability under various conditions. To assess the durability of the PSCs in challenging conditions, the long-term stability test was conducted with maintaining a controlled environment with a temperature set at 60 °C or continuous 1 sun illumination (AM 1.5G). The *Double* device maintains 86.4% of the initial PCE even after 1860 h at the thermal stress of 60 °C, indicating its robust thermal stability, as shown in Figure 2-7(c) [36-38]. Additionally, maximum power point tracking (MPPT) results are consistent with the thermal stability test, where the *Double* device exhibits endurance for 1030 h with 80.2% retention of the initial PCE at the given continuous light condition, as shown in Figure 2-7(d) [39-40]. This indicated that the double-side passivation of PTMAI improved long-term stability significantly with the increased photovoltaic performance of PSCs.

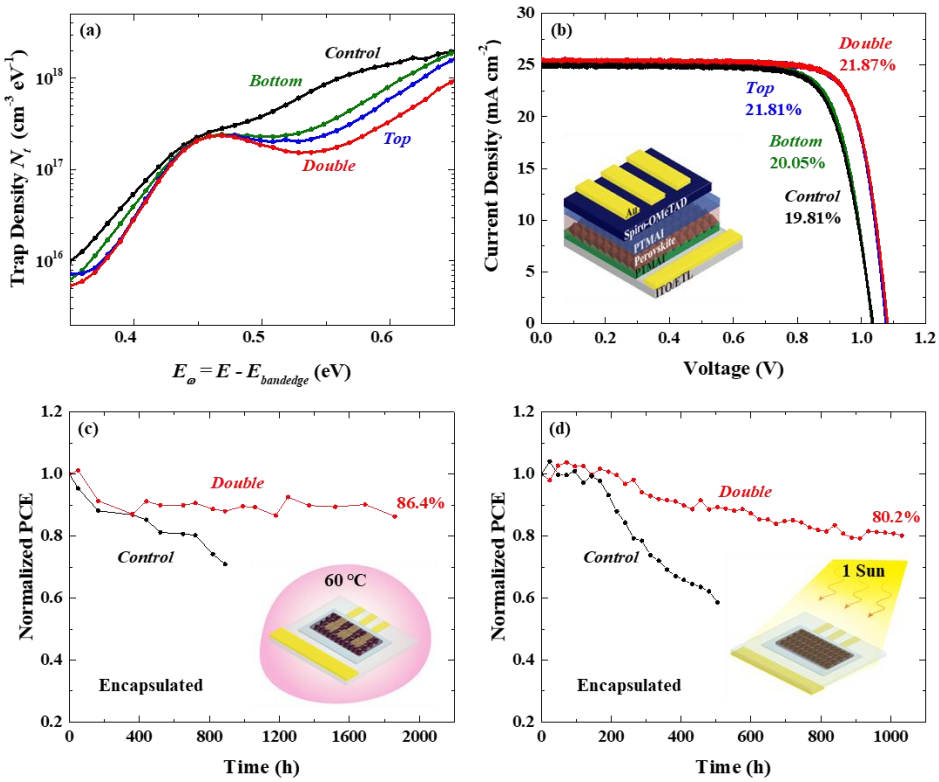

Figure 2-7. Electronic trap density, photovoltaic performance, and long-term stability for PSCs. (a) Trap density of state (tDOS) and (b) *J-V* curves of *Control*, *Bottom*, *Top*, and *Double* devices. (c,d) Long-term stability test for the encapsulated PCS devices without/with double passivation of PTMAI, under the thermal stress of 60 °C condition and continuous 1 sun illumination (AM 1.5 G).

Figure 2-8 is presented to emphasize the overall trend, resulting from the application of PTMAI passivation. In Figure 2-8(a), the trend of binding energies for Pb 4*f* and I 3*d* is depicted for various types of perovskite, revealing a consistent downward shift whenever the PTMAI layer was added. Figure 2-8(b) illustrated the changes in the root-mean-square value (σ_{rms}) and lateral grain size for the *Control*, *Bottom*, *Top*, and *Double* films, indicating that the incorporation of PTMAI makes smoother surface and larger grain size of perovskite films. The integrated peak intensity of the (001) plane increases, and the nonuniform distribution of local strains decreased with the addition of PTMAI passivation layers, as shown in Figure 2-8(c). The local strain of the *Double* film showed a remarkable decrease from 0.099% to 0.052%, which is almost half of the *Control*. Additionally, the integrated trap density (from 0.45 to 0.65 eV) decreased in the order of the *Control*, *Bottom*, *Top*, and *Double* devices, as depicted in Figure 2-8(d) [41-44]. The integrated trap density of the *Double* device incredibly decreased from 18.8×10^{16} to 6.05×10^{16} cm^{-3}, which is almost one-third of the *Control*. These overall trends provide strong evidence of the enhanced interfacial and bulk properties of perovskite, validating the efficacy of this novel double-side passivation tactic. These findings highlight the potential of this approach as a promising strategy for advancing the commercialization of perovskite-semiconductor devices.

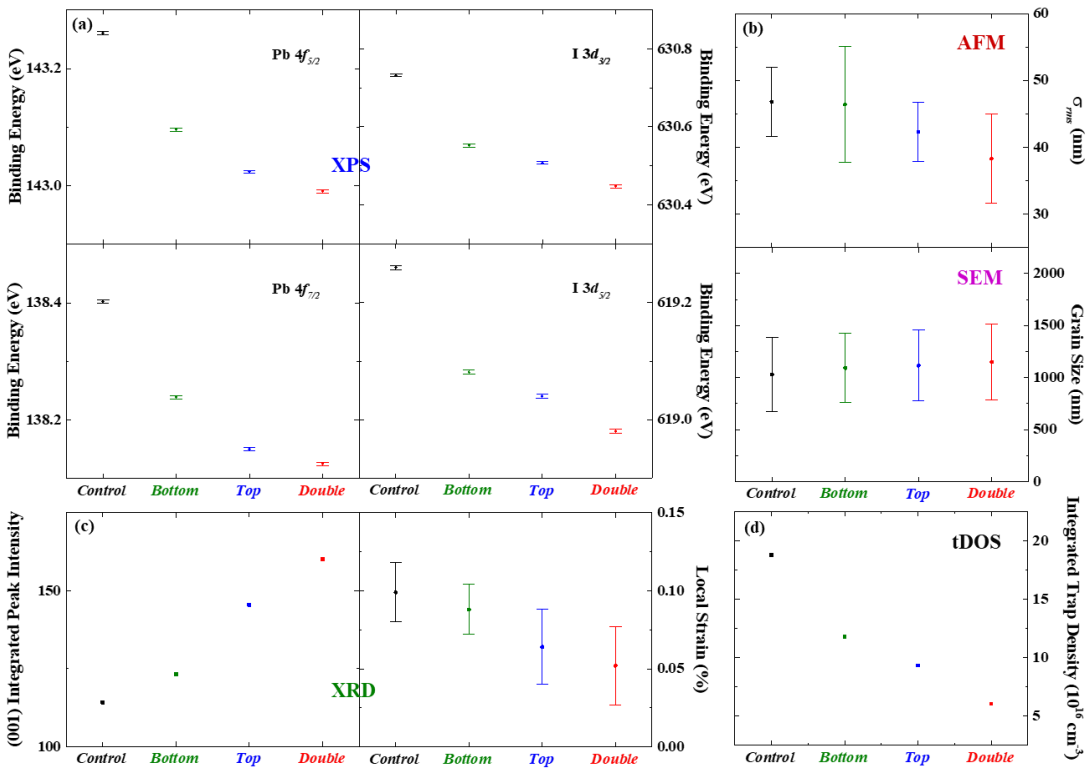

Figure 2-8. The trend of overall results obtained through the PTMAI passivation. (a) XPS spectra of Pb 4*f* and I 3*d* binding energy peak shift through PTMAI passivation (Figure 2-3). (b) Root-mean-square values of surface roughness (σ_{rms}) and grain size of perovskite films through surface topographical measurements (Figures 2-6(a), (c), and (d)). (c) The trend of (001) integrated peak intensity (Figure 2-2) and nonuniform distribution of local strains (Figure 2-5). (d) Integrated trap density of PCSs calculated from 0.45 to 0.65 eV (Figure 2-7(a)).

2.4. Conclusions

We have demonstrated a novel double-side passivation tactic to eliminate defects at both interfaces for the perovskite layer and enhance the photovoltaic performance and long-term stability of PSCs. Remarkable trap-density suppression with higher crystallinity of perovskite, larger grain, and smoother surface has resulted in outstanding reproducibility in PCE. The synergistic effect of double-side passivation of PTMAI promotes the highest PCE of 21.87% coupled with long-term stability which exhibits sustained 80.2% and 86.4% of the initial efficiency after 1030 h and 1860 h, respectively, under 1 Sun illumination (AM 1.5G) and the thermal stress of 60 °C. This straightforward double-side passivation technique utilizing multifunctional compounds like PTMAI holds great promise in enhancing the performance and stability of perovskite semiconductors for various device commercialization.

2.5. References

[1] B. Gil, J. Kim, A. J. Yun, K. Park, J. Cho, M. Park, B. Park, *Nanomaterials* **2020**, *10*, 1669.

[2] B. Lee, A. J. Yun, J. Kim, B. Gil, B. Shin, B. Park, *Adv. Mater. Interfaces* **2019**, *6*, 1901372.

[3] T. Li, Y. Pan, Z. Wang, Y. Xia, Y. Chen, W. Huang, *J. Mater. Chem. A* **2017**, *5*, 12602.

[4] B. Lee, T. Hwang, S. Lee, B. Shin, B. Park, *Sci. Rep*. **2019**, *9*, 4803.

[5] B. Lee, S. Lee, D. Cho, J. Kim, T. Hwang, K. H. Kim, S. Hong, T. Moon, B. Park, *ACS Appl*. *Mater*. *Interfaces* **2016**, *8*, 30985.

[6] Q. Jiang, Y. Zhao, X. Zhang, X. Yang, Y. Chen, Z. Chu, Q. Ye, X. Li, Z. Yin, J. You, *Nat. Photonics* **2019**, *13*, 460.

[7] J. Kim, A. J. Yun, B. Gil, Y. Lee, B. Park, *Adv. Funct. Mater*. **2019**, *29*, 1905190.

[8] T. Hwang, A. J. Yun, B. Lee, J. Kim, Y. Lee, B. Park, *J. Appl. Phys*. **2019**, *126*, 023101.

[9] X. Wang, Y. Wang, T. Zhang, X. Liu, Y. Zhao, *Angew. Chem*. *Int. Ed.* **2020**, *59*, 1469.

[10] H. Shu, J. Xia, H. Yang, J. Luo, Z. Wan, H. A. Malik, F. Han, X. Yao, C. Jia, *ACS Sustain. Chem. Eng.* **2020**, *8*, 10859.

[11] L. Gao, H. Su, Z. Xu, Y. Hu, J. Zhang, S. Liu, *Sol. RRL* **2021**, *5*, 2100416.

[12] M. Degani, Q. An, M. Albaladejo-Siguan, Y. J. Hofstetter, C. Cho, F. Paulus, G. Grancini, Y. Vaynzof, *Sci. Adv*. **2021**, *7*, eabj7930.

[13] J. Peng, J. I. Khan, W. Liu, E. Ugur, T. Duong, Y. Wu, H. Shen, K. Wang, H. Dang, E. Aydin, X. Yang, Y. Wan, K. J. Weber, K. R. Catchpole, F. Laquai, S. D. Wolf, T. P. White, *Adv. Energy Mater*. **2018**, *8*, 1801208.

[14] K. H. Girish, *Surfaces and Interfaces* **2021**, *26*, 101420.

[15] J. Cho, B. Kim, S. Ryu, A. J. Yun, B. Gil, J. Lim, J. Kim, J. Kim, B. Park, *Electron. Mater. Lett.* **2023**, DOI: 10.1007/s13391-023-00410-x.

[16] A. Binek, F. C. Hanusch, P. Docampo, T. Bein, *J. Phys. Chem. Lett*. **2015**, *6*, 1249.

[17] B.-W. Park, H. W. Kwon, Y. Lee, D. Y. Kim, M. G. Kim, G. Kim, K.-J. Kim, Y. K. Kim, J. Im, T. J. Shin, S. I. Seok, *Nat. Energy* **2021**, *6*, 419.

[18] H. Zhang, F. Ye, W. Li, J. Yao, R. S. Gurney, D. Liu, C. Xiong, T. Wang, *Organic Electronics* **2019**, *67*, 187.

[19] X. Ma, J. Pan, Y. Wang, X. Gao, M. Hu, Z. Ku, Y. Ma, F. Huang, Y.-B. Cheng, J. Lu, *Chemical Engineering Journal* **2022**, *455*, 136626.

[20] J. Kim, A. J. Yun, B. Park, J. Kim, *EcoMat* **2023**, *5*, e12314.

[21] J. Chen, J.-Y. Seo, N.-G. Park, *Adv. Energy Mater*. **2018**, *8*, 1702714.

[22] E. Akman, A. E. Shalan, F. Sadegh, S. Akin, *ChemSusChem* **2021**, *14*, 1176.

[23] D. He, X. Xu, Z. Liang, Y. Niu, Y. Sun, T. Gavin, P. Falaras, L. Hu, *J. Mater. Chem. C* **2021**, *9*, 9584.

[24] Z. Li, N. Liu, K. Meng, Z. Liu, Y. Hu, Q. Xu, X. Wang, S. Li, L. Cheng, G. Chen, *Nano Lett.* **2019**, *19*, 5237.

[25] S. Song, S. J. Yang, J. Choi, S. G. Han, K. Park, H. Lee, J. Min, S. Ryu, K. Cho, *ACS Appl. Mater. Interfaces* **2021**, *13*, 37052.

[26] J. Kim, H. Choi, C. Nahm, C. Kim, S. Nam, S. Kang, D.-R. Jung, J. I. Kim, J. Kang, B. Park, *J. Power Sources* **2012**, *220*, 108.

[27] Y. Chen, Y. Lei, Y. Li, Y. Yu, Z. Cai, M.-H. Chiu, R. Rao, Y. Gu, C. Wang, W. Choi, H. Hu, C. Wang, Y. Li, J. Song, J. Zhang, B. Qi, M. Lin, Z. Zhang, A. E. Islam, B. Maruyama, S. Dayeh, L.-J. Li, K. Yang, Y.-H. Lo, S. Xu, *Nature* **2020**, *577*, 209.

[28] T. Kim, J. Oh, B. Park, K. S. Hong, *Appl. Phys. Lett.* **2000**, *76*, 3043.

[29] B. Park, G. B. Stephenson, S. M. Allen, K. F. Ludwig Jr, *Phys. Rev. Lett.* **1992**, *68*, 1742.

[30] B. Kim, C. Kim, T.-G. Kim, D. Ahn, B. Park, *J. Electrochem. Soc.* **2006**, *153*, A1773.

[31] J. Lim, B. Gil, A. J. Yun, J. Kim, B. Park, *Appl. Energy Mater*. **2023**, *6*, 371.

[32] D.-R. Jung, D. Son, J. Kim, C. Kim, B. Park, *Appl. Phys. Lett.* **2008**, *93*, 163118.

[33] H. Min, S.-G. Ji, S. I. Seok, *Joule* **2022**, *6*, 2175.

[34] Y. Wang, T. Zhang, M. Kan, Y. Zhao, *J. Am. Chem. Soc*. **2018**, *140*, 12345.

[35] Y. Chen, J. Shi, X. Li, S. Li, X. Lv, X. Sun, Y.-Z. Zheng, X. Tao, *J. Mater. Chem. A* **2020**, *8*, 6349.

[36] X. Ling, H. Zhu, W. Xu, C. Liu, L. Pan, D. Ren, J. Yuan, B. W. Larson, C. Grätzel, A. R. Kirmani, O. Ouellette, A. Krishna, J. Sun, C. Zhang, Y. Li, S. M. Zakeeruddin, J. Gao, Y. Liu, J. R. Durrant, J. M. Luther, W. Ma, M. Grätzel, *Angew. Chem. Int. Ed.* **2021**, *60*, 27299.

[37] Y. Miao, Z. Wang, C. Chen, X. Ding, M. Zhai, L. Liu, Z. Xia, H. Wang, M. Cheng. *Sol. RRL* **2022**, *6*, 2200364.

[38] J. Jeong, M. Kim, J. Seo, H. Lu, P. Ahlawat, A. Mishra, Y. Yang, M. A. Hope, F. T. Eickemeyer, M. Kim, Y. J. Yoon, I. W. Choi, B. P. Darwich, S. J. Choi, Y. Jo, J. H. Lee, B. Walker, S. M. Zakeeruddin, L. Emsley, U. Rothlisberger, A. Hagfeldt, D. S. Kim, M. Grätzel, J. Y. Kim, *Nature* **2021**, *592*, 381.

[39] H. Lu, Y. Liu, P. Ahlawat, A. Mishra, W. R. Tress, F. T. Eickemeyer, Y. Yang, F. Fu, Z. Wang, C. E. Avalos, B. I. Carlsen, A. Agarwalla, X. Zhang, X. Li, Y. Zhan, S. M. Zakeeruddin, L. Emsley, U. Rothlisberger, L. Zheng, A. Hagfeldt, M. Grätzel, *Science* **2020**, *370*, eabb8985.

[40] G. Kim, H. Min, K. S. Lee, D. Y. Lee, S. M. Yoon, S. I. Seok, *Science*, **2020**, *370*, 108.

[41] D. B. Khadka, Y. Shirai, M. Yanagida, K. Miyano, *J. Mater. Chem. C* **2018**, *6*, 162.

[42] D. Prochowicz, P. Yadav, M. Saliba, M. Saski, S. M. Zakeeruddin, J. Lewiński, M. Grätzel, *ACS Appl. Mater. Interfaces* **2017**, *9*, 28418.

[43] A. J. Yun, B. Gil, S. Ryu, J. Kim, B. Park, *ACS Appl. Energy Mater*. **2022**, *5*, 7192.

[44] S. Lee, J. C. Flanagan, J. Kim, A. J. Yun, B. Lee, M. Shim, B. Park, *ACS Appl. Mater. Interfaces* **2019**, *11*, 19104.

Abstract in Korean

유기/무기 하이브리드 페로브스카이트 태양전지(PSC)는 탁월한 특성으로 인해 유망한 재생 에너지 소자로 각광받고 있다. 그러나 동시에 전력 변환 효율(PCE) 및 장기 안정성과 관련된 문제에 직면해 있다. PSC에서 표면 결함의 존재는 비발광 재결합 및 열화를 일으키기 때문에 높은 효율과 안정성을 달성하는 데 주요 장애물이 된다.

따라서 전하 캐리어 수송층과 페로브스카이트 층 사이의 두 인터페이스에서 전자 결함을 억제하는 것은 PSC의 광전지 성능과 장기 안정성을 향상시키는 데 필수적이다. 이 연구에서는 전자결함을 효과적으로 제거하기 위해 페닐트리메틸암모늄아이오다이드(PTMAI) 염을 이용한 새로운 양 계면 결함 제어 방법을 적용하였다. 페닐트리메틸암모늄(PTMA) 양이온은 효과적인 결함 제어 물질로서 물과 열에 대한 저항성이 있는 것으로 알려진 4차 암모늄 염이다. 또한, 이 양이온의 큰 부피는 페로브스카이트 층으로부터 페로브스카이트와 전하 수송층 사이의 인터페이스로 이온이 이동하는 것을 억제하는 데 도움이 된다.

그 결과, PTMAI를 사용한 양 계면 결함제어 방법은 페로브스카이트 층에 존재하는 국부적 응력의 불균일한 분포를 완화시켜 페로브스카이트 결정도의 향상에 기여한다. 또한 이 방법은 트랩 밀도를 현저하게 억제하여 페로브스카이트 층에서 결정 입자를 더 크게 성장시키고 표면을 더 매끄럽게 만든다. 결과적으로 PTMAI를 사용한 양 계면 결함 제어 방법으로 $FAPbI_3$ 태양전지의 효율이 크게 개선되어 21.87%의 최종적인 PCE를 달성하였다. 또한, 결함이 억제된 소자는 60 ℃의 온도 조건 하에서 1860 시간 그리고 1 Sun (AM 1.5 G)의 지속적인 광 조건 하에서 1030 시간 후에 초기 효율의 80% 이상을 유지하면서 향상된 장기 안정성을 달성하였다.

주요어: 페로브스카이트 태양전지, 결함 제어, 양 계면 결함 억제, 페닐트리메틸암모늄아이오다이드, 소자 장기 안정성

학번: 2021-29138